

# Wave-optics investigation of branch-point density

Jeffrey R. Beck,<sup>a,\*</sup> Jeremy P. Bos,<sup>a</sup> Terry J. Brennan,<sup>b</sup> and Mark F. Spencer<sup>c</sup>

<sup>a</sup>Michigan Technological University, Department of Electrical and Computer Engineering, Houghton, Michigan, United States

<sup>b</sup>Prime Plexus, Placentia, California, United States

<sup>c</sup>Air Force Research Laboratory, Directed Energy Directorate, Kirtland Air Force Base, New Mexico, United States

**Abstract.** We use wave-optics simulations to investigate branch-point density (i.e., the number of branch points within the pupil-phase function) in terms of the grid sampling. The goal for these wave-optics simulations is to model plane-wave propagation through homogeneous turbulence, both with and without the effects of a finite inner scale modeled using a Hill spectrum. In practice, the grid sampling provides a gauge for the amount of branch-point resolution within the wave-optics simulations, whereas the Rytov number, Fried coherence diameter, and isoplanatic angle provide parameters to setup and explore the associated deep-turbulence conditions. Via Monte Carlo averaging, the results show that without the effects of a finite inner scale, the branch-point density grows without bound with adequate grid sampling. However, the results also show that as the inner-scale size increases, this unbounded growth (1) significantly decreases as the Rytov number, Fried coherence diameter, and isoplanatic angle increase in strength and (2) saturates with adequate grid sampling. These findings imply that future developments need to include the effects of a finite inner scale to accurately model the multifaceted nature of the branch-point problem in adaptive optics. © *The Authors. Published by SPIE under a Creative Commons Attribution 4.0 International License. Distribution or reproduction of this work in whole or in part requires full attribution of the original publication, including its DOI.* [DOI: [10.1117/1.OE.61.4.044104](https://doi.org/10.1117/1.OE.61.4.044104)]

**Keywords:** branch points; branch cuts; atmospheric propagation; deep turbulence; adaptive optics; wave-optics simulations.

Paper 20220065G received Jan. 19, 2022; accepted for publication Mar. 24, 2022; published online Apr. 13, 2022.

## 1 Introduction

Laser-beam propagation through deep turbulence results in constructive and destructive interference known as scintillation. The Rytov number (aka log-amplitude variance) gives a gauge for the amount of scintillation. In turn, when the Rytov number increases above 0.1, the scintillation becomes severe and total-destructive interference gives rise to branch points in the pupil-phase function. These so-called branch points manifest where the real and imaginary parts of the complex-optical field equate to zero.

Branch points, in practice, add a rotational component to the phase function. This rotational component gets mapped to the null space of traditional-least-squares phase reconstruction algorithms. Due to the foundational work of Fried,<sup>1</sup> researchers appropriately refer to this rotational component as the “hidden phase.” With this last point in mind, the existence of branch points leads to unavoidable  $2\pi$  phase discontinuities known as branch cuts. These branch cuts become linked to positively and negatively charged branch points within the pupil-phase function. Because of interactuator coupling, continuous-face-sheet deformable mirrors are unable to fully compensate for the branch cuts.<sup>2-7</sup> Thus, the branch-point problem in adaptive optics tends to be the “Achilles’ heel” to beam-control systems that perform deep-turbulence phase compensation.

Fried and Vaughn were the first to study the existence of turbulence-induced branch points.<sup>8</sup> Afterward, many works began investigating the effects of branch points (aka phase

---

\*Address all correspondence to Jeffrey R. Beck, [jrbeck@mtu.edu](mailto:jrbeck@mtu.edu)

dislocations,<sup>9,10</sup> screw dislocations,<sup>11,12</sup> optical vortices,<sup>13,14</sup> etc.), which typically require the use of high-fidelity and wave-optics simulations.<sup>15–22</sup> For example, Voitsekhovich et al.<sup>23</sup> were the first to perform a wave-optics investigation of branch-point density (i.e., the number of branch points within the pupil-phase function). They did so as a function of propagation distance with the effect of a finite inner scale but for a fixed grid sampling. As previously mentioned, Fried was the first to describe the branch-point problem in terms of the hidden phase.<sup>1</sup> Since then, researchers have proposed several branch-point-tolerant phase reconstruction algorithms.<sup>24–29</sup> These algorithms, at large, have had limited degrees of success due to the multifaceted nature of the branch-point problem in adaptive optics. Most recently, members of the Starfire Optical Range at the Air Force Research Laboratory investigated the aggregate behavior of branch points,<sup>30–37</sup> and the goal being to relate the branch-point pairs received in a pupil-phase function to the upstream turbulence that created them. This work, in total, could inform the development of future branch-point-tolerant phase reconstruction algorithms. To increase the fidelity of the results, future developments need to include the effects of additive-sensor noise, low signal-to-noise ratios, and subaperture-sampling requirements.<sup>38–45</sup> With this history in mind, reformulating the problem in terms of slope discrepancy,<sup>46,47</sup> especially when accounting for the effects of speckle due to rough-surface scattering,<sup>48–51</sup> could also inform these future developments.

This paper builds on this aforementioned history. In particular, it uses wave-optics simulations to investigate the branch-point density as a function of the grid sampling. The goal for these wave-optics simulations is to model plane-wave propagation through homogeneous turbulence, both with and without the effects of a finite inner scale modeled using a Hill spectrum. In practice, the Rytov number, Fried coherence diameter, and isoplanatic angle help to setup and explore the associated deep-turbulence conditions. These parameters provide a gauge for the amount of scintillation, turbulence-limited resolution, and anisoplanatism, respectively, within the wave-optics simulations. On the other hand, the grid sampling provides a gauge for the amount of branch-point resolution within the wave-optics simulations.

Via Monte Carlo averaging, the results show that without the effects of a finite inner scale, the branch-point density grows without bound with adequate grid sampling. Even so, as the inner-scale size increases, the results also show that this unbounded growth (1) significantly decreases as the Rytov number, Fried coherence diameter, and isoplanatic angle increase in strength and (2) saturates with adequate grid sampling. These findings are encouraging from the standpoint that they could readily improve the performance of existing branch-point-tolerant phase reconstruction algorithms, as well as inform the development of future algorithms.

It is important to note that this paper also builds on the work contained in a recent conference proceeding.<sup>52</sup> The main difference is that this paper includes the effects of a finite inner scale. Both papers show that the branch-point density grows without bound when neglecting the effects of a finite inner scale. This finding speaks to a preconceived notion within the atmospheric-propagation research community that the branch-point density grows without bound with increasing branch-point resolution. Nonetheless, the results of this paper ultimately show that if one includes the effects of a finite inner scale, then this unbounded growth (1) significantly decreases as the associated deep-turbulence conditions become more pronounced and (2) saturates with adequate branch-point resolution within the wave-optics simulations. These findings are novel and worth sharing with the atmospheric-propagation research community. In general, (1) and (2) imply that future developments need to include the effects of a finite inner scale to accurately model the multifaceted nature of the branch-point problem in adaptive optics.

In what follows, Sec. 2 provides the background details needed to use the branch-point density as a metric of interest. Section 3 provides the wave-optics simulation details needed to setup and explore the associated deep-turbulence conditions, which assume plane-wave propagation through homogeneous turbulence. Results and discussion naturally follow in Sec. 4 with a conclusion in Sec. 5.

## 2 Background

In the pupil plane of an optical system, the complex-optical field,  $U$ , takes the following phasor form:

$$U = A \exp(-j\phi), \quad (1)$$

where  $A$  is the pupil-amplitude function and  $\phi$  is the pupil-phase function, such that

$$\phi = \text{Arg}(U) = \tan^{-1} \left[ \frac{\text{Im}(U)}{\text{Re}(U)} \right]. \quad (2)$$

Here,  $\text{Re}(U)$  and  $\text{Im}(U)$  are the real and imaginary components of  $U$ . Substituting Eq. (1) into Eq. (2) results in a modulo- $2\pi$  function that researchers often refer to as the “principle value” or “wrapped phase.” When  $A = 0$ , the argument of  $U$  is indeterminate and therefore a multi-valued function.<sup>12</sup> This outcome corresponds to the case where  $\text{Re}(U) = \text{Im}(U) = 0$  and is the reason branch points arise within  $\phi$  due to total-destructive interference.

Researchers can determine the location of a branch point using a contour integral around the the gradient of the pupil-phase function,  $\nabla\phi$ .<sup>1</sup> Specifically, when the following relationship holds true:

$$\oint_C \nabla\phi \cdot d\mathbf{r} = \pm 2\pi(N_+ - N_-), \quad (3)$$

$\nabla\phi$  is no longer homogeneous and  $\phi$  is no longer a purely potential field. In Eq. (3),  $N_+$  is the number of positive branch points and  $N_-$  is the number of negative branch points within  $\phi$ .

The sign of the closed-loop contour integration in the clockwise direction determines the overall polarity in Eq. (3). Due to this convention, one can determine the number of branch points,  $N_{BP}$ , in an  $N \times M$  grid, viz,

$$N_{BP} = \sum_{n=1}^N \sum_{m=1}^M \left| \frac{1}{2\pi} \left[ \begin{array}{l} (\phi_{n,m} - \phi_{n,m+1}) - (\phi_{n+1,m+1} - \phi_{n+1,m}) \\ -(\phi_{n,m+1} - \phi_{n+1,m+1}) + (\phi_{n+1,m} - \phi_{n,m}) \end{array} \right] \right|, \quad (4)$$

where  $N + 1 = 1$  and  $M + 1 = 1$ . Equation (4) says that if one first breaks the  $N \times M$  grid into a series of  $2 \times 2$  subgrids and sums up the phase difference around each set of four grid points (in the clockwise direction), then a positive  $2\pi$  value results in a positive branch point and a negative  $2\pi$  value results in a negative branch point. To determine  $N_{BP}$ , one then sums up the total number of positive and negative branch points.

These aforementioned sums, as written in Eq. (4), include what Fried refers to as spurious branch points.<sup>1</sup> In practice, spurious branch points are a pair of positive and negative branch points centered on immediately adjacent grid points. This outcome is undesirable because the associated branch cut remains unresolved and could be the result of an artifact within the wave-optics simulations. To address these concerns, one can use a simple search to remove the spurious branch points from the sums in Eq. (4). Empirical evidence says that spurious branch points make up a significant portion of the total number of positive and negative branch points—~40% on average. Thus, in this paper, we present all results with spurious branch points removed.

With results in mind, the branch-point density,  $\mathcal{D}_{BP}$  is the metric of interest in this paper. As such

$$\mathcal{D}_{BP} = \frac{N_{BP}}{\pi(D/2)^2}, \quad (5)$$

where  $D$  is the circular-pupil diameter. Simply put,  $\mathcal{D}_{BP}$  is the number of branch points within the pupil-phase function.

### 3 Setup and Exploration

The wave-optic simulations performed in this paper made use of the WavePlex Toolbox for MATLAB.<sup>53</sup> This toolbox uses the split-step beam propagation method (BPM) to simulate the propagation of monochromatic and polychromatic light through the atmosphere.<sup>15–22</sup> In practice, the split-step BPM divides the atmosphere into independent volumes, such that a phase screen

represents the atmospheric aberrations present in a volume. Angular-spectrum propagation to each phase screen (from the source plane to the pupil plane) then represents the propagation of light through the atmosphere. With the split-step BPM in mind, this section provides the setup and exploration needed to appreciate the results presented in the next section.

### 3.1 Setup

Table 1 contains a summary of all the parameters of interest in the wave-optics simulations. The goal for these wave-optics simulations was to model plane-wave propagation through homogeneous turbulence. For this purpose, the wave-optics simulations made use of  $N \times N$  grids, where  $N$  is the grid resolution. The physical side length,  $S$ , was the same in both the source and pupil planes, allowing for unity scaling within the setup. With that said, the source plane was setup with a plane wave of unit irradiance and the pupil plane was setup with a circular-pupil diameter,  $D$ . For the minimum grid resolution used within the wave-optics simulations, the setup also satisfied critical sampling,<sup>16</sup> such that  $N_{\min} = S^2/(\lambda Z) = 512$ , where  $N_{\min}$  is the minimum grid resolution,  $\lambda$  is the wavelength, and  $Z$  is the propagation distance. The overall setup resulted in a substantial guard band ratio (GBR), where  $\text{GBR} = S/D$ . Such a GBR helped in combating the effects of aliasing,<sup>15,16</sup> which we determined to be visually negligible within the wave-optics simulations for all  $N$ . The overall setup also resulted in a grid sampling,  $\delta(N)$ , where

$$\delta(N) = \frac{S}{N}. \quad (6)$$

As such,  $\delta(N)$  provided a gauge for the amount of branch-point resolution within the wave-optics simulations.

While Table 1 contains all the parameters of interest in the wave-optics simulations, Table 2 makes use of several path-integral expressions to define the deep-turbulence conditions. These path-integral expressions were the subject of a recent conference proceeding that discusses the limitations of deep turbulence.<sup>54</sup> For compactness, Table 2 contains a representative subset of these deep-turbulence conditions, which consisted of Rytov numbers ranging from 0.1 to 10.0 in increments of 0.1.

Recall that the Rytov number provides a gauge for the amount of scintillation. Given plane-wave propagation,<sup>15</sup> the path-integral expression takes the following form:

$$\mathcal{R}_{PW} = 0.563k^{7/6} \int_0^Z C_n^2(z)(Z-z)^{5/6} dz, \quad (7)$$

where  $C_n^2(z)$  is the path-dependent refractive index structure coefficient and  $k = 2\pi/\lambda$  is the angular wavenumber. With homogeneous turbulence, the path-integral expression reduces to a closed-form expression, where

$$\mathcal{R}_{PW} = 2.62 \frac{C_n^2 Z^{11/6}}{\lambda^{7/6}}. \quad (8)$$

**Table 1** Parameters of interest in the wave-optics simulations.

Parameters (MKS units)	Symbol	Value(s)
Grid resolution	$N$	512 to 16, 384
Side length (m)	$S$	1.6
Wavelength (m)	$\lambda$	$1 \times 10^{-6}$
Propagation distance (m)	$Z$	$5 \times 10^3$
Aperture diameter (m)	$D$	0.2
Guard band ratio	GBR	8
Grid sampling (m)	$\delta(N)$	$3.1 \times 10^{-3} - 9.8 \times 10^{-5}$

**Table 2** Representative subset of the deep-turbulence conditions.

$\mathcal{R}_{PW}$	$C_n^2$ (m <sup>-2/3</sup> )	$D/r_{0,PW}$	$\theta_0/(\lambda/D)$
0.1	$6.31 \times 10^{-16}$	2.15	2.10
0.2	$1.26 \times 10^{-15}$	3.26	1.38
0.3	$1.89 \times 10^{-15}$	4.16	1.09
0.4	$2.53 \times 10^{-15}$	4.94	0.91
0.5	$3.16 \times 10^{-15}$	5.65	0.80
0.6	$3.79 \times 10^{-15}$	6.30	0.72
0.7	$4.42 \times 10^{-15}$	6.91	0.65
0.8	$5.05 \times 10^{-15}$	7.48	0.60
0.9	$5.68 \times 10^{-15}$	8.03	0.56
1.0	$6.31 \times 10^{-15}$	8.56	0.53
2.0	$1.26 \times 10^{-14}$	12.97	0.35
3.0	$1.89 \times 10^{-14}$	16.54	0.27
4.0	$2.53 \times 10^{-14}$	19.66	0.23
5.0	$3.16 \times 10^{-14}$	22.47	0.20
6.0	$3.79 \times 10^{-14}$	25.07	0.18
7.0	$4.42 \times 10^{-14}$	27.50	0.16
8.0	$5.05 \times 10^{-14}$	29.80	0.15
9.0	$5.68 \times 10^{-14}$	31.98	0.14
10.0	$6.31 \times 10^{-14}$	34.06	0.13

Also recall that when the Rytov number increases above 0.1, the scintillation becomes severe and total-destructive interference gives rise to branch points in the pupil-phase function. Thus, when  $0.1 < \mathcal{R}_{PW} \leq 0.5$ ,  $0.5 < \mathcal{R}_{PW} \leq 1$ , and  $\mathcal{R}_{PW} > 1$ , one is left with weak-to-moderate, moderate-to-strong, and strong scintillation conditions, respectively.<sup>54</sup>

For completeness in defining the deep-turbulence conditions, Table 2 also includes values for the Fried coherence diameter and the isoplanatic angle. Given plane-wave propagation through homogeneous turbulence,<sup>15</sup> the path-integral expressions reduce to closed-form expressions, such that

$$r_{0,PW} = \left[ 0.423k^2 \int_0^Z C_n^2(z) dz \right]^{-3/5} \Rightarrow 0.185 \frac{\lambda^{6/5}}{(C_n^2)^{3/5} Z^{3/5}}, \quad (9)$$

for the Fried coherence diameter, and

$$\theta_0 = \left[ 2.91k^2 \int_0^Z C_n^2(z)(Z-z)^{5/3} dz \right]^{-3/5} \Rightarrow 0.105 \frac{\lambda^{6/5}}{(C_n^2)^{3/5} Z^{8/5}}, \quad (10)$$

for the isoplanatic angle. For all intents and purposes, the Fried coherence diameter helps in parameterizing resolution, whereas the isoplanatic angle helps in parameterizing anisoplanatism.<sup>55</sup> Thus, when  $D/r_{0,PW} > 1$  and  $\theta_0/(\lambda/D) < 10$ , one is left with turbulence-limited resolution and anisoplanatic aberrations, respectively.<sup>54</sup>

In what follows, we present an exploration of the deep-turbulence conditions provided in Table 2, both with and without the effects of a finite inner scale. In particular, we use the

well-known Kolmogorov spectrum when the wave-optics simulations do not include the effects of a finite inner scale. This spectrum is an idealization with an inner-scale size,  $\ell_0$ , of zero and an outer-scale size,  $L_0$ , of infinity. Such a spectrum does not give an accurate representation of the actual energy distribution in a turbulent volume.<sup>15</sup> This shortcoming can be remedied by using a modified spectrum such as the Hill spectrum.<sup>56</sup> Specifically, this paper makes use of the Hill spectrum because it includes a small rise at high wavenumbers near  $1/\ell_0$ , and it is readily available within the WavePlex Toolbox for MATLAB.

### 3.2 Exploration

Figures 1 and 2 show the numerical log-amplitude variance,  $\sigma_\chi^2$ , as a function of the analytical Rytov number,  $\mathcal{R}_{PW}$ . In particular, Fig. 1 corresponds to the first half of the deep-turbulence conditions setup in Table 2, whereas Fig. 2 corresponds to all of the deep-turbulence conditions setup in Table 2. Both figures include this scintillation-strength exploration for the minimum grid sampling,  $\delta(N = 512) = \delta_{\min}$ , and the maximum grid sampling,  $\delta(N = 16,384) = \delta_{\max}$ , within the wave-optics simulations (cf. Table 1). Both figures also include this scintillation-strength exploration for values of 3.1, 6.2, 12.4, and 24.8 mm for the inner-scale size,  $\ell_0$ . These values represent finite inner scales equal to one, two, four, and eight times  $\delta_{\min}$ , respectively.

Due to the limitations of the Rytov approximation,<sup>57</sup> the strength of the scintillation is often split into two regimes with respect to  $\mathcal{R}_{PW}$ . Specifically, the weak-scintillation regime occurs when  $\mathcal{R}_{PW} \leq 0.25$ , and the strong-scintillation regime occurs when  $\mathcal{R}_{PW} > 0.25$ . One can clearly see both regimes in Figs. 1 and 2 with  $\mathcal{R}_{PW} \approx 0.25$  serving as an inflection point with respect to  $\sigma_\chi^2$ . Beyond this inflection point,  $\sigma_\chi^2$  heads into a saturated regime.<sup>58</sup> This saturation process reaches another inflection point when  $\mathcal{R}_{PW} \approx 1$ . Beyond this second inflection point,  $\sigma_\chi^2$  heads into a supersaturated regime.<sup>58</sup>

It is important to note that Fig. 1 highlights the saturated regime when  $\mathcal{R}_{PW} > 0.25$ , whereas Fig. 2 highlights the supersaturated regime when  $\mathcal{R}_{PW} > 1$ . These regimes are nominally the same for both  $N = 512$  and  $N = 16,384$  and for all values of  $\ell_0/\delta_{\min}$ . Thus, Figs. 3 and 4 show the normalized irradiance (top row), wrapped phase (middle row), and branch-point density (bottom row) for a single realization of Kolmogorov turbulence with  $N = 512$  (left column)

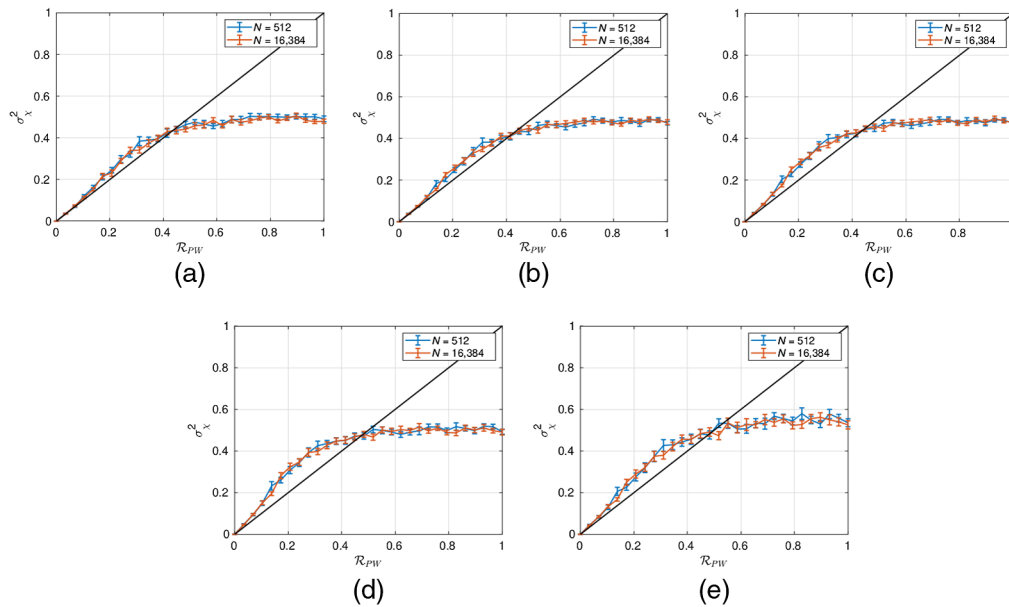


**Fig. 1** Log-amplitude variance ( $\sigma_\chi^2$ ) as a function of Rytov number ( $\mathcal{R}_{PW}$ ) for the first half of Table 2. In (a)  $\ell_0/\delta_{\min} = 0$ , (b)  $\ell_0/\delta_{\min} = 1$ , (c)  $\ell_0/\delta_{\min} = 2$ , (d)  $\ell_0/\delta_{\min} = 4$ , and (e)  $\ell_0/\delta_{\min} = 8$ . Note that the plotted lines represent the Monte Carlo averages associated with 100 turbulence realizations, and the error bars represent the standard deviations. Also note that the solid black lines denote where  $\sigma_\chi^2 = \mathcal{R}_{PW}$ .

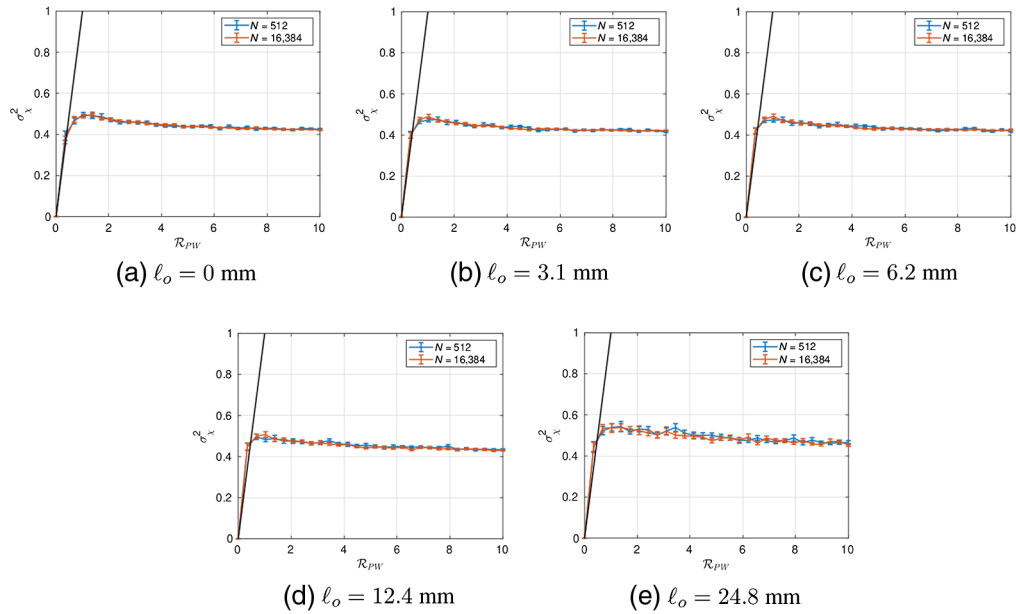


**Fig. 2** Log-amplitude variance ( $\sigma_{\chi^2}$ ) as a function of Rytov number ( $\mathcal{R}_{PW}$ ) for all of Table 2. In (a)  $\ell_o/\delta_{\min} = 0$ , (b)  $\ell_o/\delta_{\min} = 1$ , (c)  $\ell_o/\delta_{\min} = 2$ , (d)  $\ell_o/\delta_{\min} = 4$ , and (e)  $\ell_o/\delta_{\min} = 8$ . Note that the plotted lines represent the Monte Carlo averages associated with 100 turbulence realizations, and the error bars represent the standard deviations. Also note that the solid black lines denote where  $\sigma_{\chi^2} = \mathcal{R}_{PW}$ .

and  $N = 16,384$  (right column). Figure 3 corresponds to the first inflection point, where  $\mathcal{R}_{PW} = 0.25$ , and Fig. 4 corresponds to the second inflection point, where  $\mathcal{R}_{PW} = 1$ .

Figures 3 and 4 show how the branch-point density,  $\mathcal{D}_{BP}$ , increases as a function of increasing Rytov number,  $\mathcal{R}_{PW}$ , and as a function of increasing grid sampling,  $\delta(N)$ . Comparing both figures together illustrates how  $\mathcal{D}_{BP}$  increases from the first inflection point,  $\mathcal{R}_{PW} = 0.25$ , to the second inflection point,  $\mathcal{R}_{PW} = 1$ , whereas comparing the left and right columns in each figure separately illustrates how  $\mathcal{D}_{BP}$  increases from the minimum grid sampling,  $\delta(N = 512) = \delta_{\min}$ , to the maximum grid sampling,  $\delta(N = 16,384) = \delta_{\max}$ . These outcomes confirm that  $\mathcal{R}_{PW}$  provides a gauge for the amount of scintillation within the wave-optics simulations. On the other hand,  $\delta(N)$  provides a gauge for the amount of branch-point resolution within the wave-optics simulations.

## 4 Results and Discussion

The results presented in this section show that without the effects of a finite inner scale, the branch-point density grows without bound with adequate grid sampling. In addition, the results show that as the inner-scale size increases this unbounded growth (1) significantly decreases as the Rytov number, Fried coherence diameter, and isoplanatic angle increase and (2) saturates with adequate grid sampling. To make these findings manifest, we discuss the relevant trends in the figures that follow.

In support of (1), Figs. 5–7 show the branch-point density,  $\mathcal{D}_{BP}$ , as a function of the Rytov number,  $\mathcal{R}_{PW}$ , the circular-pupil diameter relative to the Fried coherence diameter,  $D/r_{0,PW}$ , and the isoplanatic angle relative to the diffraction-limited half angle,  $\theta_0/(\lambda/D)$ , respectively. The legends in each subplot denote the grid resolutions,  $N$ , setup in Table 1. Each subplot also uses the same inner-scale size relative to the minimum grid sampling,  $\ell_o/\delta_{\min}$ , explored in Figs. 1 and 2. In Figs. 5–7, the plotted lines represent the Monte Carlo averages associated with 100 turbulence realizations, and the error bars represent the standard deviations. Similar to Figs. 1 and 2, the width of the error bars are small (at most 4% of the mean) and thus we believe that 100 Monte Carlo realizations are adequate in quantifying the behavior of  $\mathcal{D}_{BP}$  in terms of  $\mathcal{R}_{PW}$ ,  $D/r_{0,PW}$ , and  $\theta_0/(\lambda/D)$ .

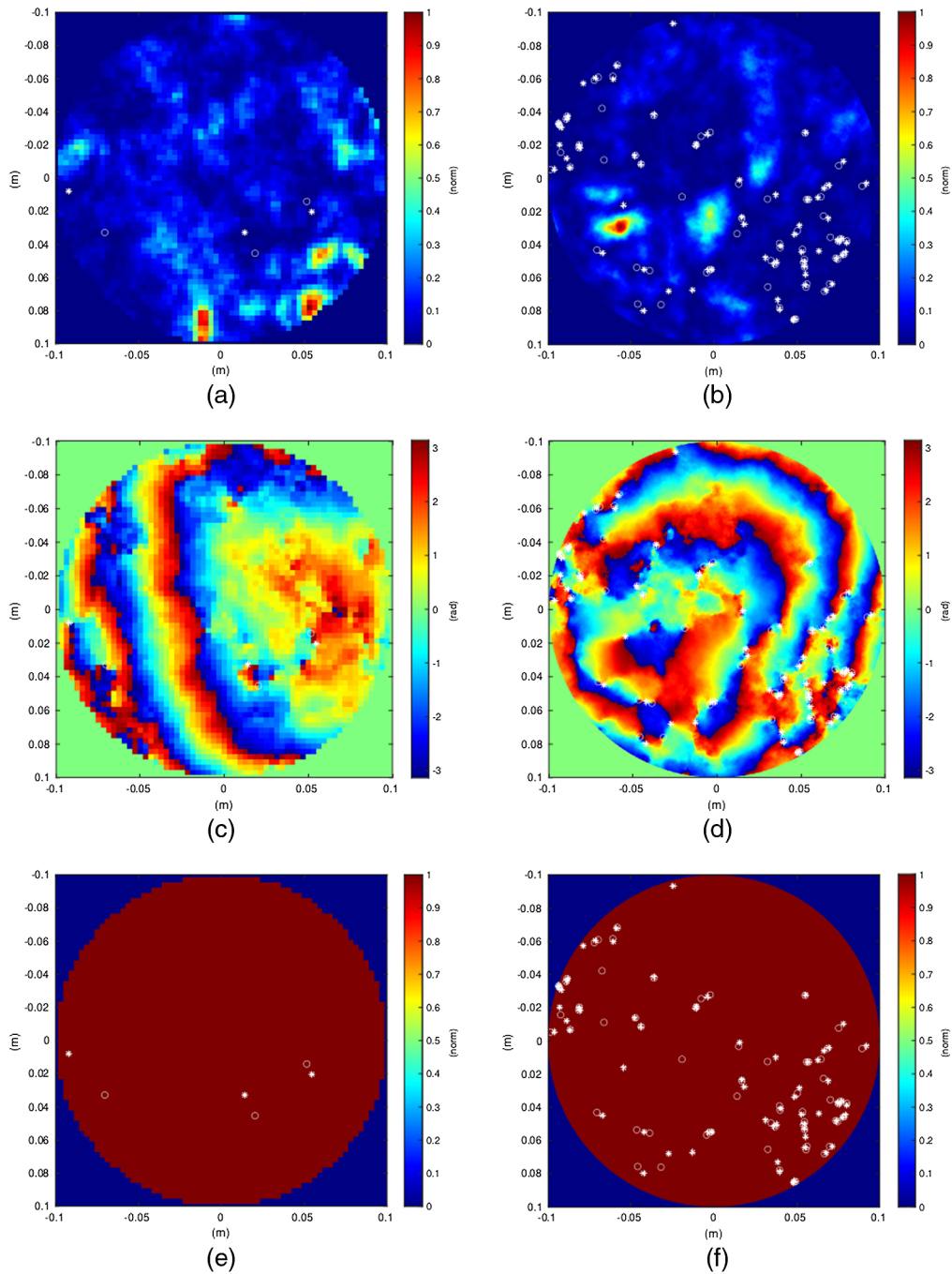


**Fig. 3** Single realization of Kolmogorov turbulence, where  $\mathcal{R}_{PW} = 0.25$ . The asterisks denote the location of the positive branch points, and the circles denote the location of the negative branch points. Note that  $N = 512$  in left column and  $N = 16,384$  in the right column. Also note that the top row illustrates the normalized irradiance, the middle row illustrates the wrapped phase, and bottom row illustrates the branch-point density.

In Fig. 5(a), where  $\ell_0/\delta_{\min} = 0$ , we see that as  $\mathcal{R}_{PW}$  increases,  $\mathcal{D}_{BP}$  increases linearly without bound when  $N > 2048$ . Figures 5(b)–5(e), on the other hand, show that when  $\ell_0$  increases, this unbounded linear growth significantly decreases. In particular, when  $\ell_0/\delta_{\min} > 2$  and  $N > 2048$ , the results for  $\mathcal{D}_{BP}$  tend to overlap, whereas when  $\ell_0/\delta_{\min} \leq 2$  and  $N \leq 2048$ , the results for  $\mathcal{D}_{BP}$  tend to saturate.

In Fig. 6(a), where  $\ell_0/\delta_{\min} = 0$ , we see that as  $D/r_{0,PW}$  increases,  $\mathcal{D}_{BP}$  increases exponentially without bound when  $N > 2048$ . Figures 6(b)–6(e), on the other hand, show that when

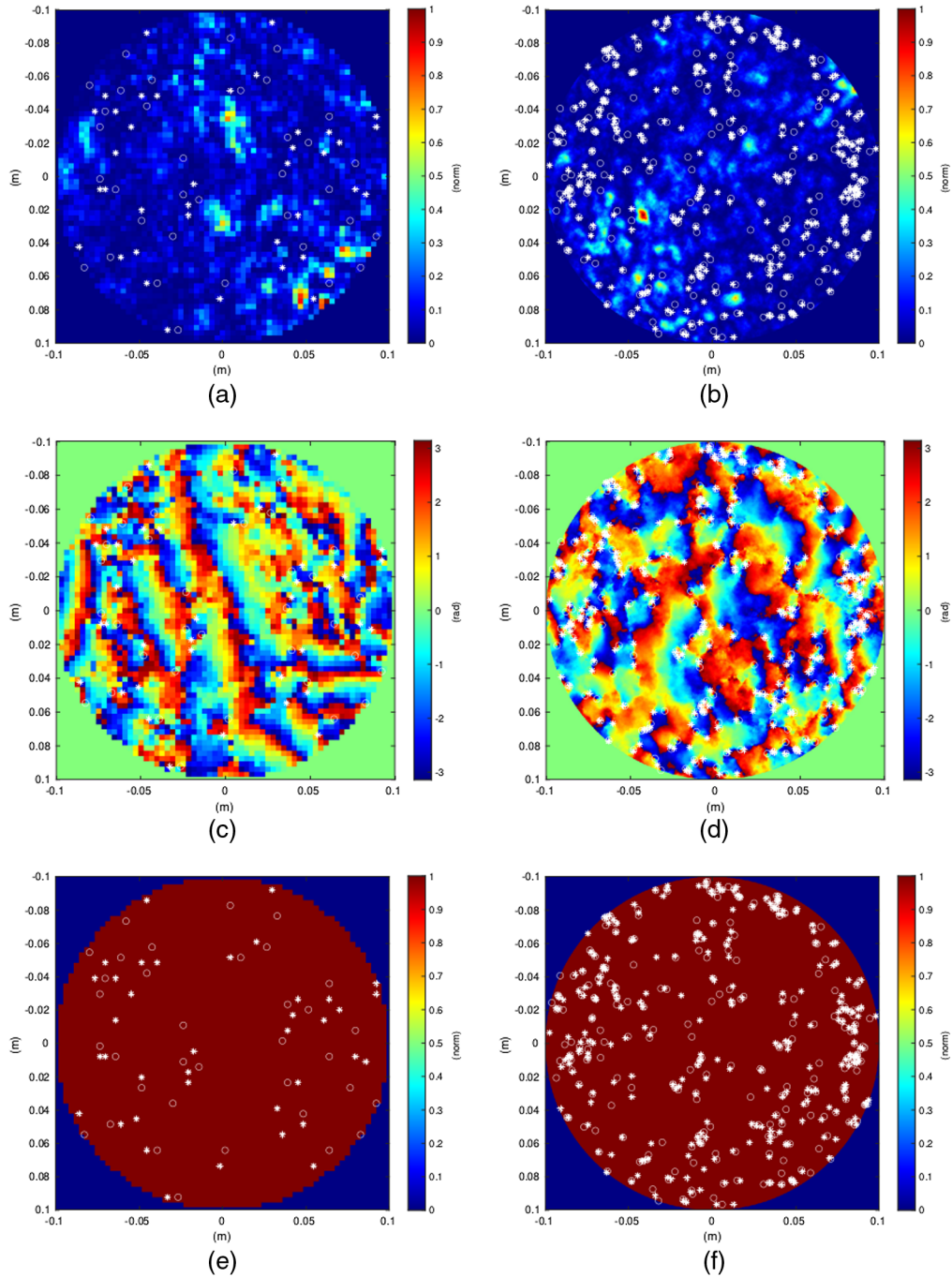


**Fig. 4** Single realization of Kolmogorov turbulence, where  $\mathcal{R}_{PW} = 1.0$ . The asterisks denote the location of the positive branch points, and the circles denote the location of the negative branch points. Note that  $N = 512$  in left column and  $N = 16,384$  in the right column. Also note that the top row illustrates the normalized irradiance, the middle row illustrates the wrapped phase, and bottom row illustrates the branch-point density.

$\ell_0$  increases, this unbounded exponential growth significantly decreases. In particular, when  $\ell_0/\delta_{\min} > 2$  and  $N > 2048$ , the results for  $\mathcal{D}_{BP}$  tend to overlap, whereas when  $\ell_0/\delta_{\min} \leq 2$  and  $N \leq 2048$ , the results for  $\mathcal{D}_{BP}$  tend to saturate.

In Fig. 7(a), where  $\ell_0/\delta_{\min} = 0$ , we see that as  $\theta_0/(\lambda/D)$  decreases,  $\mathcal{D}_{BP}$  increases exponentially without bound when  $N > 2048$ . Figures 7(b)–7(e), on the other hand, show that when  $\ell_0$  increases, this unbounded exponential growth significantly decreases. In particular, when

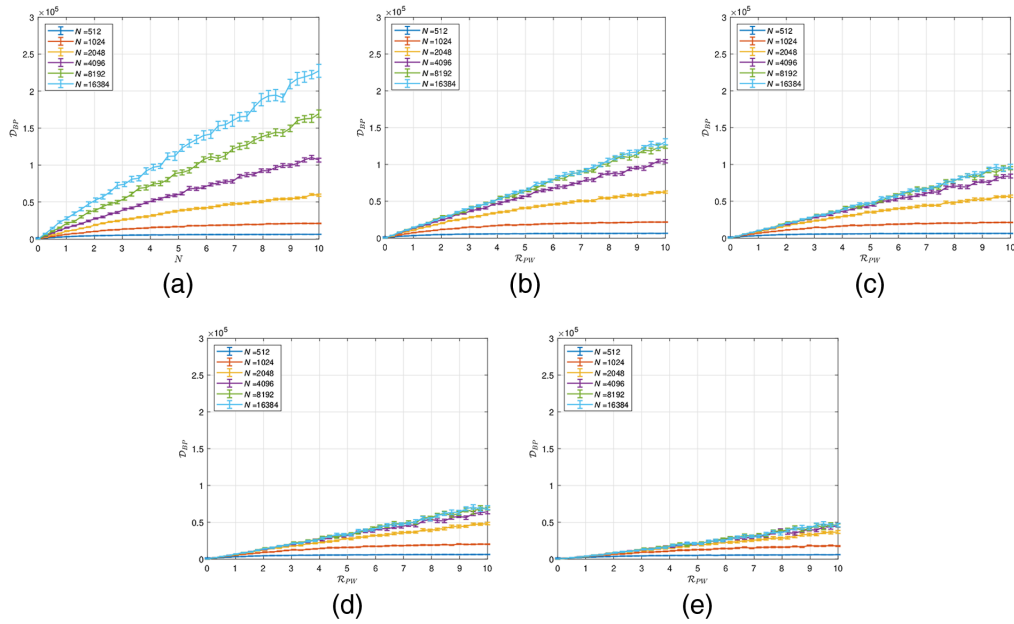


**Fig. 5** Branch point density ( $D_{BP}$ ) as a function of Rytov number ( $\mathcal{R}_{PW}$ ) for the grid resolutions ( $N$ ) setup in Table 1. In (a)  $\ell_o/\delta_{\min} = 0$ , (b)  $\ell_o/\delta_{\min} = 1$ , (c)  $\ell_o/\delta_{\min} = 2$ , (d)  $\ell_o/\delta_{\min} = 4$ , and (e)  $\ell_o/\delta_{\min} = 8$ .

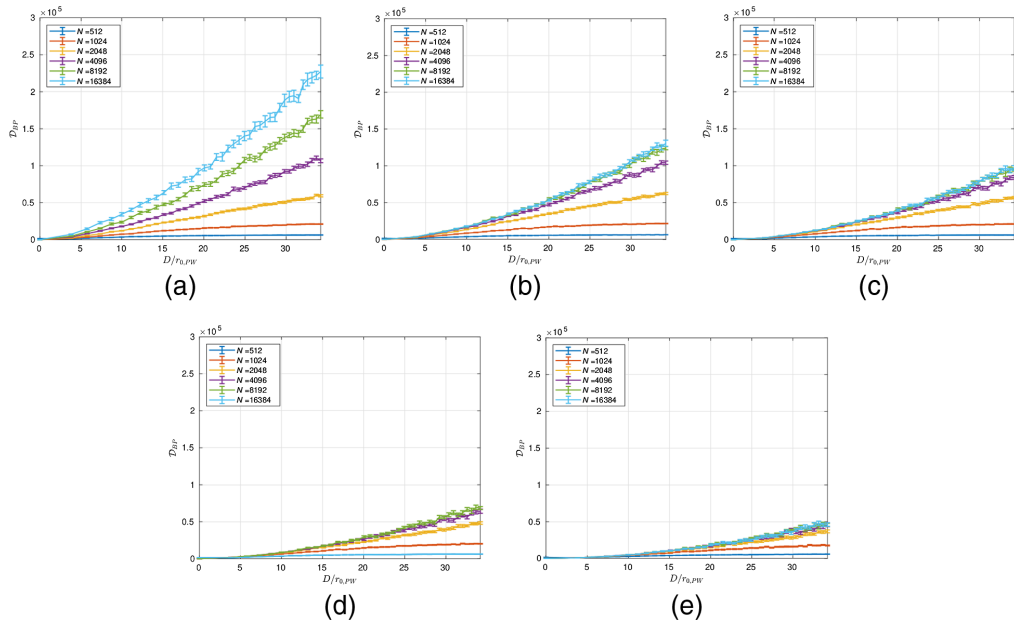


**Fig. 6** Branch point density ( $D_{BP}$ ) as a function of circular-pupil diameter relative to Fried coherence length ( $D/r_0$ ) for the grid resolutions ( $N$ ) setup in Table 1. In (a)  $\ell_o/\delta_{\min} = 0$ , (b)  $\ell_o/\delta_{\min} = 1$ , (c)  $\ell_o/\delta_{\min} = 2$ , (d)  $\ell_o/\delta_{\min} = 4$ , and (e)  $\ell_o/\delta_{\min} = 8$ .

$\ell_o/\delta_{\min} > 2$  and  $N > 2048$ , the results for  $D_{BP}$  tend to overlap, whereas when  $\ell_o/\delta_{\min} \leq 2$  and  $N \leq 2048$ , the results for  $D_{BP}$  tend to saturate.

The aforementioned saturation in Figs. 5–7 when  $N \leq 2048$  is due to inadequate sampling of the turbulent volume and is not physical. One rule of thumb says that the Fried coherence diameter relative to the grid sampling needs to be greater than ten (i.e.,  $r_{0,PW}/\delta(N) > 10$ ). Simply put, when  $N \leq 2048$ , we do not always satisfy this rule of thumb within the wave-optics simulations, as shown in Figs. 5–7.

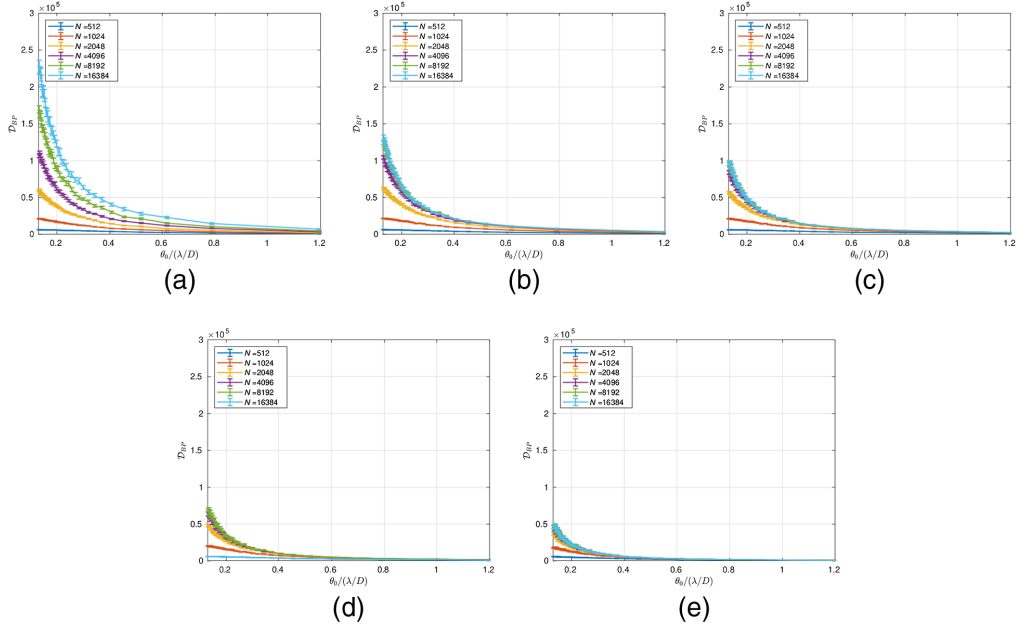


**Fig. 7** Branch point density ( $\mathcal{D}_{BP}$ ) as a function of isoplanatic angle relative to the diffraction-limited half angle ( $\theta_0/(\lambda/D)$ ) for the grid resolutions ( $N$ ) setup in Table 1. In (a)  $\ell_0/\delta_{\min} = 0$ , (b)  $\ell_0/\delta_{\min} = 1$ , (c)  $\ell_0/\delta_{\min} = 2$ , (d)  $\ell_0/\delta_{\min} = 4$ , and (e)  $\ell_0/\delta_{\min} = 8$ .

In support of (2), Fig. 8 shows the branch-point density,  $\mathcal{D}_{BP}$ , as a function of the grid resolution,  $N$ . The legends in each subplot denote the Rytov numbers,  $\mathcal{R}_{PW}$ , setup in Table 2. Each subplot also uses the same inner-scale size relative to the minimum grid sampling,  $\ell_0/\delta_{\min}$ , explored in Figs. 5–7. In Fig. 8, the plotted lines represent the Monte Carlo averages associated with 100 turbulence realizations, and the error bars represent the standard deviations. Similar to Figs. 5–7, the width of the error bars are small (at most 4% of the mean) and thus we believe that 100 Monte Carlo realizations are adequate in quantifying the behavior of  $\mathcal{D}_{BP}$  in terms of  $N$ .

In Fig. 8(a), where  $\ell_0/\delta_{\min} = 0$ , we see that as  $N$  increases,  $\mathcal{D}_{BP}$  increases without bound for all  $\mathcal{R}_{PW}$ . Figures 8(b)–8(e), on the other hand, show that when  $\ell_0/\delta_{\min}$  increases, this unbounded growth saturates. In particular, when  $\ell_0/\delta_{\min} > 0$  and  $N > 2048$ , the results for  $\mathcal{D}_{BP}$  tend to roll over, whereas when  $\ell_0/\delta_{\min} \leq 2$  and  $N \leq 2048$ , the results for  $\mathcal{D}_{BP}$  tend to grow monotonically. This monotonic growth increases as  $\mathcal{R}_{PW}$  increases, which again is most likely caused by insignificant sampling of the turbulent volume.

Figure 8 ultimately shows that as  $\ell_0/\delta_{\min}$  increases,  $\mathcal{D}_{BP}$  increasingly saturates when  $N > 2048$ . This result disagrees with a preconceived notion within the atmospheric-propagation community that the branch-point density grows without bound with increasing branch-point resolution. As shown in Fig. 8(a), this preconceived notion is the result of using the well-known Kolmogorov spectrum within the wave-optics simulations. Recall that this spectrum is an idealization with an inner-scale size,  $\ell_0$ , of zero and an outer-scale size,  $L_0$ , of infinity. Such a spectrum leads to energy distribution beyond the inertial sub range, which is not physical. Also recall that this shortcoming can be remedied using a modified spectrum such as the Hill spectrum.<sup>56</sup> In so doing, the wave-optics simulations more accurately model the energy distribution in a turbulent volume and lead to the results presented in Figs. 8(b)–8(e). With this last point in mind, Ref. 55 recently showed that wave-optics simulations need to include the effects of a finite outer scale to accurately model the effects of anisoplanatism.

## 5 Conclusions

This paper used wave-optics simulations to investigate the branch-point density in terms the grid sampling. The goal for these wave-optics simulations was to model plane-wave propagation through homogeneous turbulence, both with and without the effects of a finite inner scale

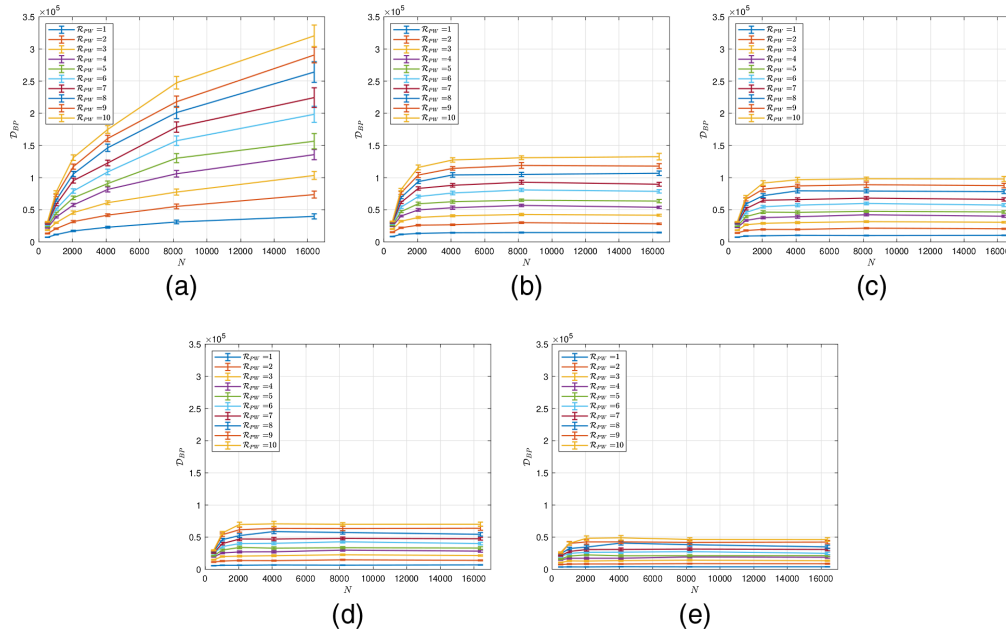


**Fig. 8** Branch point density ( $\mathcal{D}_{BP}$ ) as a function of grid resolution ( $N$ ) for the plane-wave Rytov numbers ( $\mathcal{R}_{PW}$ ) setup in Table 2. In (a)  $\ell_o/\delta_{\min} = 0$ , (b)  $\ell_o/\delta_{\min} = 1$ , (c)  $\ell_o/\delta_{\min} = 2$ , (d)  $\ell_o/\delta_{\min} = 4$ , and (e)  $\ell_o/\delta_{\min} = 8$ .

modeled using a Hill spectrum. In practice, the Rytov number, Fried coherence diameter, and isoplanatic angle provided parameters to setup and explore the associated deep-turbulence conditions within the wave-optics simulations. The grid sampling, on the other hand, provided a gauge for the amount of branch-point resolution within the wave-optics simulations. Via Monte Carlo averaging, the results showed that without the effects of a finite inner scale, the branch-point density grew without bound. Nevertheless, the results also showed that as the inner-scale size increased, this unbounded growth (1) significantly decreased as the associated deep-turbulence conditions became more pronounced and (2) saturated with adequate branch-point resolution within the wave-optics simulations.

The results of this paper imply that future developments need to include the effects of a finite inner scale to accurately model the multifaceted nature of the branch-point problem in adaptive optics. Recall that this problem tends to be the ‘‘Achilles’ heel’’ to beam-control systems that perform deep-turbulence phase compensation. Thus, the results of this paper are encouraging from the standpoint that they could readily improve the performance of existing branch-point-tolerant phase reconstruction algorithms. The results of this paper could also inform the development of future branch-point-tolerant phase reconstruction algorithms, which take into account the effects of additive-sensor noise, low signal-to-noise ratios, and subaperture-sampling requirements. These future developments are a critical next step to improving the performance of beam-control systems that perform deep-turbulence phase compensation.

## Acknowledgments

The authors would like to thank the Joint Directed Energy Transition Office for sponsoring this research. Approved for public release; distribution is unlimited. Public Affairs release approval #AFRL-2022-0153.

## References

1. D. L. Fried, ‘‘Branch point problem in adaptive optics,’’ *J. Opt. Soc. Am. A* **15**(10), 2759–2768 (1998).

2. J. D. Barchers, D. L. Fried, and D. J. Link, "Evaluation of the performance of Hartmann sensors in strong scintillation," *Appl. Opt.* **41**(6), 1012–1021 (2002).
3. J. D. Barchers, D. L. Fried, and D. J. Link, "Evaluation of the performance of a shearing interferometer in strong scintillation in the absence of additive measurement noise," *Appl. Opt.* **41**(18), 3674–3684 (2002).
4. J. D. Barchers et al., "Performance of wavefront sensors in strong scintillation," *Proc. SPIE* **4839**, 217–227 (2003).
5. M. Vorontsov et al., "Comparative efficiency analysis of fiber-array and conventional beam director systems in volume turbulence," *Appl. Opt.* **55**, 4170–4185 (2016).
6. M. F. Spencer and T. J. Brennan, "Compensation in the presence of deep turbulence using tiled-aperture architectures [invited]," *Proc. SPIE* **10194**, 1019403 (2017).
7. M. T. Banet and M. F. Spencer, "Compensated-beacon adaptive optics using least-squares phase reconstruction," *Appl. Opt.* **28**, 36902–36914 (2020).
8. D. L. Fried and J. L. Vaughn, "Branch cuts in the phase function," *Appl. Opt.* **31**(15), 2865–2882 (1992).
9. V. Tartakovsky, "Phase dislocations and minimal-phase representation of the wave function," *Atmos. Ocean. Opt.* **8**, 231–234 (1995).
10. V. Tartakovsky, "Phase dislocations and focal spot," *Atmos. Ocean. Opt.* **9**, 926–929 (1996).
11. J. F. Nye and M. V. Berry, "Dislocations in wave trains," *Proc. R. Soc. Lond. A. Math. Phys. Sci.* **336**(1605), 165–190 (1974).
12. V. P. Lukin and B. V. Fortes, *Adaptive Beaming and Imaging in the Turbulent Atmosphere*, SPIE Press, Bellingham, Washington (2002).
13. G. J. Gbur, *Mathematical Methods for Optical Physics and Engineering*, Cambridge University Press, New York (2011).
14. J. W. Goodman, *Speckle Phenomena in Optics: Theory and Applications*, 2nd ed., SPIE Press, Bellingham, Washington (2020).
15. J. D. Schmidt, *Numerical Simulation of Optical Wave Propagation with Examples in MATLAB*, SPIE Press, Bellingham, Washington (2010).
16. D. G. Voelz, *Computational Fourier Optics: A MATLAB Tutorial*, SPIE Press, Bellingham, Washington (2011).
17. J. P. Bos and M. C. Roggemann, "Technique for simulating anisoplanatic image formation over long horizontal paths," *Opt. Eng.* **51**(10), 101704 (2012).
18. R. C. Hardie et al., "Simulation of anisoplanatic imaging through optical turbulence using numerical wave propagation with new validation analysis," *Opt. Eng.* **56**(7), 071502 (2017).
19. N. R. Van Zandt et al., "Polychromatic wave-optics models for image-plane speckle. 1. Well-resolved objects," *Appl. Opt.* **57**(15), 4090–4102 (2018).
20. N. R. Van Zandt et al., "Polychromatic wave-optics models for image-plane speckle. 2. Unresolved objects," *Appl. Opt.* **57**(15), 4103–4110 (2018).
21. M. F. Spencer, "Wave-optics investigation of turbulence thermal blooming interaction: I. Using steady-state simulations," *Opt. Eng.* **59**(8), 081804 (2020).
22. M. F. Spencer, "Wave-optics investigation of turbulence thermal blooming interaction: II. Using time-dependent simulations," *Opt. Eng.* **59**(8), 081805 (2020).
23. V. V. Voitsekovich, D. Kouznetsov, and D. K. Morozov, "Density of turbulence-induced phase dislocations," *Appl. Opt.* **37**(21), 4525–4535 (1998).
24. W. W. Arrasmith, "Branch-point-tolerant least-squares phase reconstructor," *J. Opt. Soc. Am. A* **16**(7), 1864–1872 (1999).
25. M. C. Roggemann and A. C. Koivunen, "Wave-front sensing and deformable-mirror control in strong scintillation," *J. Opt. Soc. Am. A* **17**(5), 911–919 (2000).
26. D. L. Fried, "Adaptive optics wave function reconstruction and phase unwrapping when branch points are present," *Opt. Commun.* **200**(1–6), 43–72 (2001).
27. T. M. Venema and J. D. Schmidt, "Optical phase unwrapping in the presence of branch points," *Opt. Exp.* **16**(10), 6985–6998 (2008).
28. M. J. Steinbock, M. W. Hyde, and J. D. Schmidt, "LSPV+7, a branch-point-tolerant reconstructor for strong turbulence adaptive optics," *Appl. Opt.* **53**(18), 3821–3831 (2014).

29. J. J. Kim, B. Fernandez, and B. Agrawal, "Iterative wavefront reconstruction for strong turbulence using Shack–Hartmann wavefront sensor measurements," *J. Opt. Soc. Am. A* **38**(3), 456–464 (2021).
30. D. W. Oesch, D. J. Sanchez, and C. L. Matson, "The aggregate behavior of branch points—measuring the number and velocity of atmospheric turbulence layers," *Opt. Exp.* **18**(21), 22377–22392 (2010).
31. D. J. Sanchez and D. W. Oesch, "Orbital angular momentum in optical waves propagating through distributed turbulence," *Opt. Exp.* **19**(24), 24596–24608 (2011).
32. D. J. Sanchez and D. W. Oesch, "Localization of angular momentum in optical waves propagating through turbulence," *Opt. Exp.* **19**(25), 25388–25396 (2011).
33. D. W. Oesch et al., "Aggregate behavior of branch points: characterization in wave optical simulation," *Opt. Eng.* **51**(10), 106001 (2012).
34. D. W. Oesch, D. J. Sanchez, and C. M. Tewksbury-Christle, "Aggregate behavior of branch points-persistent pairs," *Opt. Exp.* **20**(2), 1046–1059 (2012).
35. D. W. Oesch and D. J. Sanchez, "Creating well-defined orbital angular momentum states with a random turbulent medium," *Opt. Exp.* **20**(11), 12292–12302 (2012).
36. D. W. Oesch et al., "Creation of photonic orbital angular momentum by distributed volume turbulence," *Opt. Exp.* **21**(5), 5440–5455 (2013).
37. D. Oesch and D. Sanchez, "Photonic orbital angular momentum in starlight," *Astron. Astrophys.* **567**, A114 (2014).
38. B. M. Welsh and C. S. Gardner, "Performance analysis of adaptive-optics systems using laser guide stars and sensors," *J. Opt. Soc. Am. A* **6**(12), 1913–1923 (1989).
39. B. M. Welsh et al., "Fundamental performance comparison of a Hartmann and a shearing interferometer wave-front sensor," *J. Opt. Soc. of Am. A* **34**(21), 4186–4195 (1995).
40. T. A. Rhoadarmer and J. D. Barchers, "Noise analysis for complex field estimation using a self-referencing interferometer wave front sensor," *Proc. SPIE* **4825**, 215–227 (2002).
41. J. D. Barchers and T. A. Rhoadarmer, "Evaluation of phase-shifting approaches for a point-diffraction interferometer with the mutual coherence function," *Appl. Opt.* **41**, 7499–7509 (2002).
42. M. F. Spencer et al., "Deep-turbulence wavefront sensing using digital-holographic detection in the off-axis image plane recording geometry," *Opt. Eng.* **56**(3), 031213 (2016).
43. M. T. Banet, M. F. Spencer, and R. A. Raynor, "Digital-holographic detection in the off-axis pupil plane recording geometry for deep-turbulence wavefront sensing," *Appl. Opt.* **57**(3), 465–475 (2018).
44. D. E. Thornton, M. F. Spencer, and G. P. Perram, "Deep-turbulence wavefront sensing using digital holography in the on-axis phase shifting recording geometry with comparisons to the self-referencing interferometer," *Appl. Opt.* **58**(5), A179–A189 (2019).
45. D. E. Thornton, M. T. Banet, and M. F. Spencer, "Subaperture sampling for digital-holography applications involving atmospheric turbulence," *Appl. Opt.* **60**(25), G30–G39 (2021).
46. G. A. Tyler, "Reconstruction and assessment of the least-squares and slope discrepancy components of the phase," *J. Opt. Soc. of Am. A* **17**(10), 1828–1839 (2000).
47. T. J. Brennan, "Anatomy of the slope discrepancy structure function: characterization of turbulence," *Proc. SPIE* **5078**, 103–114 (2003).
48. N. R. Van Zandt, M. F. Spencer, and S. T. Fiorino, "Speckle mitigation for wavefront sensing in the presence of weak turbulence," *Appl. Opt.* **58**(9), 2300–2310 (2019).
49. N. R. Van Zandt and M. F. Spencer, "Improved adaptive-optics performance using polychromatic speckle mitigation," *Appl. Opt.* **59**(4), 1071–1081 (2020).
50. D. J. Burrell et al., "Wave-optics simulation of dynamic speckle: I. In a pupil plane," *Appl. Opt.* **60**(25), G64–G76 (2018).
51. D. J. Burrell et al., "Wave-optics simulation of dynamic speckle: II. In an image plane," *Appl. Opt.* **60**(25), G77–G90 (2018).
52. J. R. Beck et al., "Investigation of branch-point density using traditional wave-optics techniques," *Proc. SPIE* **10772**, 1077206 (2018).
53. T. J. Brennan is the sole author of the WavePlex Toolbox for MATLAB with correspondence to the following address: Prime Plexus, 650 N Rose Drive, #439, Placentia, CA, USA 92870.

54. M. F. Spencer, "Limitations of the deep-turbulence problem [invited]," in *Proc. Opt.*, p. PW3F.1 (2021).
55. J. R. Beck and J. P. Bos, "Angular anisoplanatism in non-Kolmogorov turbulence over horizontal paths," *J. Opt. Soc. Am. A* **37**(12), 1937–1949 (2020).
56. R. Hill and S. Clifford, "Modified spectrum of atmospheric temperature fluctuations and its application to optical propagation," *J. Opt. Soc. Am.* **68**(7), 892–899 (1978).
57. R. J. Sasiela, *Electromagnetic Wave Propagation in Turbulence: Evaluation and Application of Mellin Transforms*, 2nd ed., SPIE Press, Bellingham, Washington (2007).
58. G. R. Osche, *Optical Detection Theory for Laser Applications*, Wiley, Hoboken, New Jersey (2002).

**Jeffrey R. Beck** is a recent graduate from the Department of Electrical and Computer Engineering at Michigan Technological University and is currently seeking a postdoctoral position. He is a member of SPIE.

**Jeremy P. Bos** is an assistant professor of Electrical and Computer Engineering at Michigan Technological University. He is a senior member of SPIE.

**Terry J. Brennan** is the owner of Prime Plexus, a small business dedicated to the development of wave-optics simulations. He is a member of SPIE.

**Mark F. Spencer** is a senior physicist at the Air Force Research Laboratory, Directed Energy Directorate (AFRL/RD) and currently serves as the directed energy staff specialist at the US Indo-Pacific Command (as a liaison from AFRL/RD). He is a fellow of SPIE.